Metallography, Microstructure, and Analysis (2022) 11:736–745
https://doi.org/10.1007/s13632-022-00900-8

PEER-REVIEWED PAPER

Microstructural and Mechanical Properties of Ti-B_4C/CNF Functionally Graded Materials

Abdualkarim Musbah M. Gariba[1] · **Serkan Islak**[2] · **Husain Rajab Husain Hraam**[3] · **Mehmet Akkaş**[2]

Received: 23 July 2022 / Revised: 6 October 2022 / Accepted: 11 October 2022 / Published online: 24 October 2022

Abstract

This study aims to investigate the microstructural and mechanical properties of titanium (Ti) matrix boron carbide (B_4C) + carbon nanofiber (CNF)-reinforced functional-graded materials (FGMs) produced using the powder metallurgy method. B_4C was added to the Ti matrix at different rates, namely, 5, 10, and 15% by volume, and CNF was added at a rate of 0.5% by volume. The effect of B_4C and CNF on the properties of these composite layers was then investigated. In addition, the mechanical properties of the FGMs were compared with the mechanical properties of non-layered structures. In addition, the microstructural, phase formation, hardness, and transverse rupture strength properties of the samples were investigated in detail. The microstructural investigation revealed that the B_4C and CNF were homogeneously distributed throughout the Ti matrix and that the layers had bonded properly. With the addition of B_4C and CNF, the hardness of the materials increased significantly. The transverse rupture strengths of the FGMs were higher than those of the non-layered samples (with the exception of pure Ti), indicating that the middle layers increased the toughness of the materials.

Keywords FGMs · Ti · B_4C · CNF · Sintering

Introduction

Scientific studies on improving the properties of materials used in tools and equipment for advanced technological applications are rapidly gaining attention. As a result, new types of material are emerging, such as a new generation of functionally graded materials (FGMs). FGMs consist of varied compositions of layered components and can be tailored to ensure that their thermal and mechanical properties are optimal [1, 2].

Ceramic-based materials, which have low density, high strength, and high thermal resistance, are used in applications where high surface hardness is required. Metal-based materials have high toughness, electrical conductivity, and high workability and are used when surface hardness can be low. FGMs are designed to transition from ceramic-based regions to metals through gradual or continuous grading. The compositions, microstructures, and certain mechanical properties of these materials exhibit smooth transitions throughout their structures, providing the designer with great advantages in the production of materials with specific mechanical and thermal properties. FGMs are preferred in many applications for these reasons [3, 4].

In general, FGM structures are used frequently in the aerospace industry, electronics industry, and medical applications, especially those that operate at high temperatures. Composites with metal and ceramic structures should have high strength and hardness and exhibit high wear, thermal resistance, and fracture toughness. FGM production varies depending on the design required. The powder metallurgy method is preferred because it facilitates the use of a wide range of materials during production. In the first step of the powder metallurgy method, the powders are weighed according to the desired dimensions and then mixed. In the next step, the mixed powders are added to a pre-determined mold, and stacking-compression follows. In the last step of the manufacturing process, sintering is applied to allow the FGM to reach its full density [5, 6].

✉ Serkan Islak
serkan@kastamonu.edu.tr

[1] Department of Mechanical Engineering, Higher Institute of Science and Technology, Al-Khoms, Libya

[2] Department of Mechanical Engineering, Faculty of Engineering and Architecture, Kastamonu University, 37150 Kastamonu, Turkey

[3] Department of Mechanical Engineering, Faculty of Engineering, Elmergib University, Al-Khoms, Libya

Titanium matrix composite (TMC) materials have excellent mechanical properties, including high specific strength, high specific hardness, excellent abrasion resistance, and high temperature resistance. Therefore, they are attractive for many industries, including the aviation, automotive, chemical, and biochemical industries [7–9]. Ceramics such as Cr_3C_2, TiC, TiN, TiO_2, Si_3N_4, SiC, TiB_2, TiB, Al_2O_3, and B_4C are widely used as reinforcements in the production of TMC materials. In addition, carbon nanotubes and nanofibers have recently been used as reinforcements [10, 11]. While these ceramics, nanotubes, and fibers increase the strength of these materials considerably, they decrease their ductility and toughness [12]. FGMs can be used to produce materials with both high strength and satisfactory ductility and toughness properties. In this study, FGMs featuring Ti matrices and boron carbide and carbon nanofiber reinforcements were produced using the powder metallurgy method. The microstructural and mechanical properties of these FGMs were then thoroughly investigated. The novelty of this work is to produce FGM, which is hard on the outside and ductile on the inside. The increase in hardness on the outside was planned with the addition of B_4C, and the increase in TRS values was planned with the addition of CNF. There is no study in the literature that includes the FGM design in this composition.

Experimental Studies

In this study, titanium (Ti) was used as the matrix, and boron carbide (B_4C) and carbon nanofiber (CNF) were used as reinforcements for the FGMs. Ti powder—with 99% purity and a < 45 µm size range; B_4C powder—with 99% purity and a < 45 µm size range; and CNF powder—with 98% purity and a 100 nm × 20–200 µm (D × L) size range were purchased from the Sigma- Aldrich Company. The properties of these powders are given in Table 1, whereas the SEM images and XRD patterns of the powders are shown in Fig. 1. Note that the Ti powder is irregularly shaped (partially spongy), the B_4C powder has a sharp angular shape, and the CNF powder has a fiber-like shape. The XRD patterns indicate that there was no oxide formation in the powders prior to production.

FGMs are usually produced in three layers. Here, the outer layers are comprised of Ti-B_4C + CNF, while the middle layer consist of Ti only. The FGM compositions and those of normal materials are given in Table 2. The sample components were weighed on a precision scale and mixed in using a Turbula mixer (Celmak Makine Ltd. Co., Turkey) according to the compositions shown in Table 2. The samples were subjected to mixing for 45 min, then compressed to sheets of dimension 24 mm × 10 mm × 4.5 mm under 500 MPa of pressure in a Specac GS15011 hydraulic pellet press with a capacity of 25 tons at the Kastamonu University Central Research Laboratory. In the FGMs, the thickness of the sheets was adjusted to 1.5 mm.

Table 1 Purity and grain size values of powders

Powders	Ti	B_4C	CNF
Grain size	< 45 µm	< 45 µm	D × L 100 nm × 20–200 µm
Purity (%)	99	99	> 98

The pressed samples were sintered in a tube furnace (Protherm) in an atmosphere of protective argon gas (approximately 3 bar) of approximately 99.0% purity for 1 h at 1300 ℃ and a temperature increase rate of 10 ℃/min at the Metallurgical and Materials Engineering Laboratories of Kastamonu University. The experimental densities of the samples were measured using Archimedes' principle. The hardness measurements of the materials were done using a SHIMADZU HMV-G21 microhardness measurement device with a 10-s waiting time and 200-g load. The three-point bending tests, which were carried out to determine the transverse rupture strengths (TRSs) of the samples, were done on a universal tensile machine with a capacity of 50 kN at test speeds of 1 mm/min. Scanning electron microscopy (SEM) and energy-dispersive spectrometry (EDS) were used to examine the microstructures and fracture surfaces of the samples. X-ray diffraction (XRD) was used to determine phase formation within the samples.

Results and Discussion

In Fig. 2, macro images of FGM sample 1 are provided that are representative of the FGMs in this study. Each layer is approximately 1.5 mm in thickness. While the upper and lower layers have a Ti-5 vol% B_4C composite structure, the middle layer consists of pure titanium—these layers have bonded sufficiently. No cracks are present in the macro image; however, fluctuations are present in the inter-layer composition line. These fluctuations are thought to be caused by compression during cold pressing. In the SEM images of the 5, 10, and 15% B_4C-reinforced Ti-matrix FGM materials presented in Fig. 3, adequate bonding between the layers is also noticeable. As the B_4C ratio increases, the three-layer structure becomes more evident.

Figure 4 shows detailed SEM images of the Ti-10% B_4C-0.5 CNF FGM. As in Fig. 3, compatible bonding between the layers is present (Fig. 4a). When the composite layer is examined, it can be seen that the B_4C particles are homogeneously dispersed within the Ti matrix (Fig. 4b), indicating sufficient mixing. CNFs cannot be observed at low magnification rates, but they can be easily seen at higher

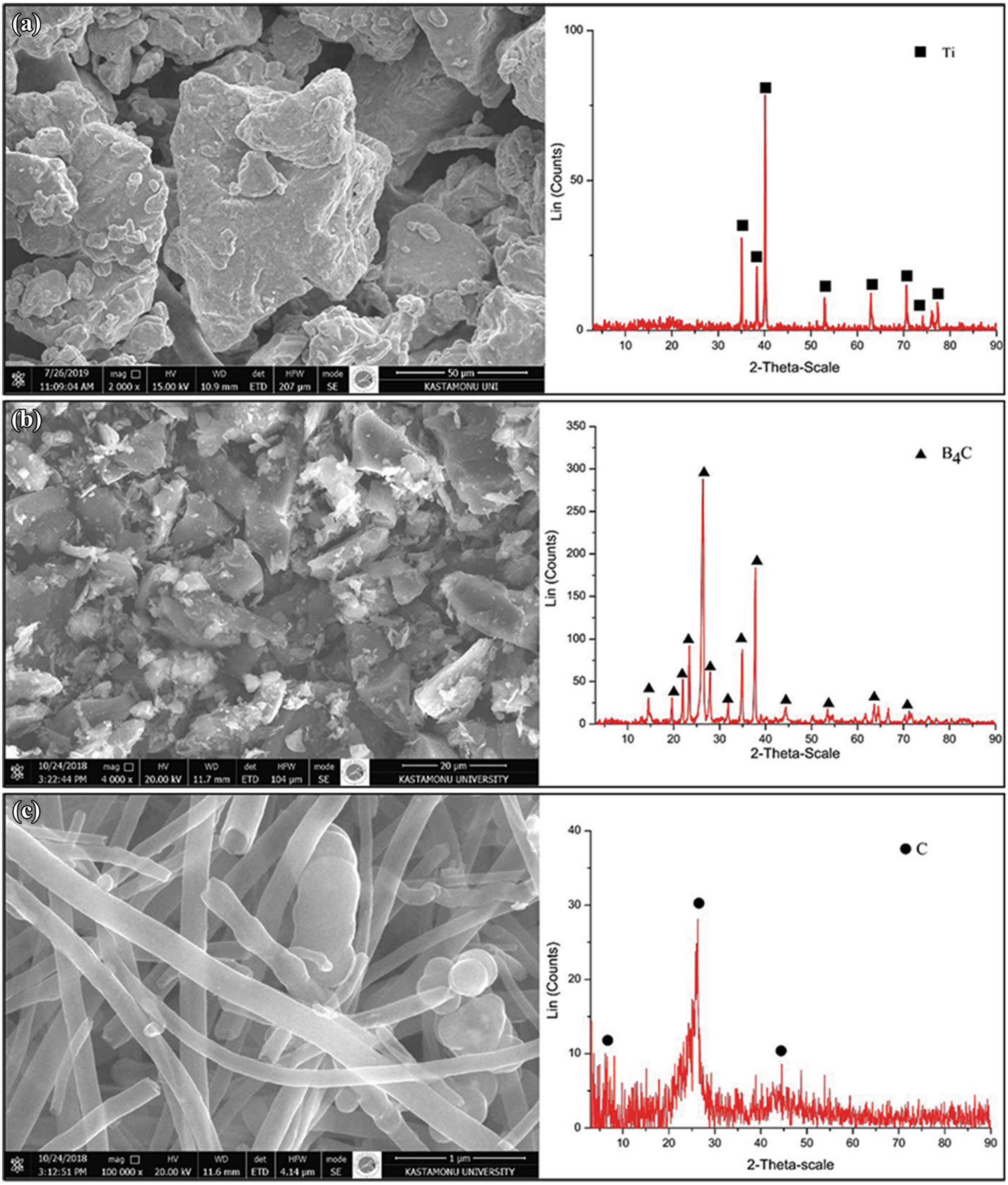

Fig. 1 SEM images and XRD patterns of powders: (**a**) Ti, (**b**) B_4C, and (**c**) CNF

magnifications (Fig. 4c and d). Although the determination cannot be made that CNFs are homogeneously distributed within the microstructure, when the SEM image in Fig. 4c is examined, it can be seen that the CNF material is distributed homogeneously. In some previous studies, the clustering of carbon nanofibers has occurred within the matrix [13]. It can

Table 2 Composition design of samples

Samples	Upper layer	Middle layer	Lower layer
1	Ti-5 vol% B_4C	Ti	Ti-5 vol% B_4C
2	Ti-10 vol% B_4C	Ti	Ti-10 vol% B_4C
3	Ti-15 vol% B_4C	Ti	Ti-15 vol% B_4C
4	Ti-5 vol% B_4C-0.5 vol% CNF	Ti	Ti-5 vol% B_4C-0.5 vol% CNF
5	Ti-10 vol% B_4C-0.5 vol% CNF	Ti	Ti-10 vol% B_4C-0.5 vol% CNF
6	Ti-15 vol% B_4C-0.5 vol% CNF	Ti	Ti-15 vol% B_4C-0.5 vol% CNF
7	Ti		
8	Ti-5 vol% B_4C		
9	Ti-5 vol% B_4C-0.5 vol% CNF		

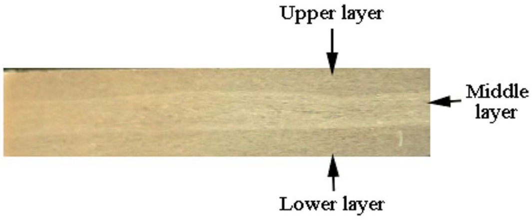

Fig. 2 Macro images of FGM sample 1

also be seen from the SEM image that the CNFs penetrate into the Ti matrix within the microstructure (Fig. 4d). The presence of pores in the microstructure of the composite layer is also noteworthy. However, this presence is commonplace in materials produced using powder metallurgy [14]. A general EDS analysis of the composite layer of Ti-10% B_4C-0.5 CNF FGM is shown in Fig. 5. The chemical composition in the EDS analysis shows the elements involved in

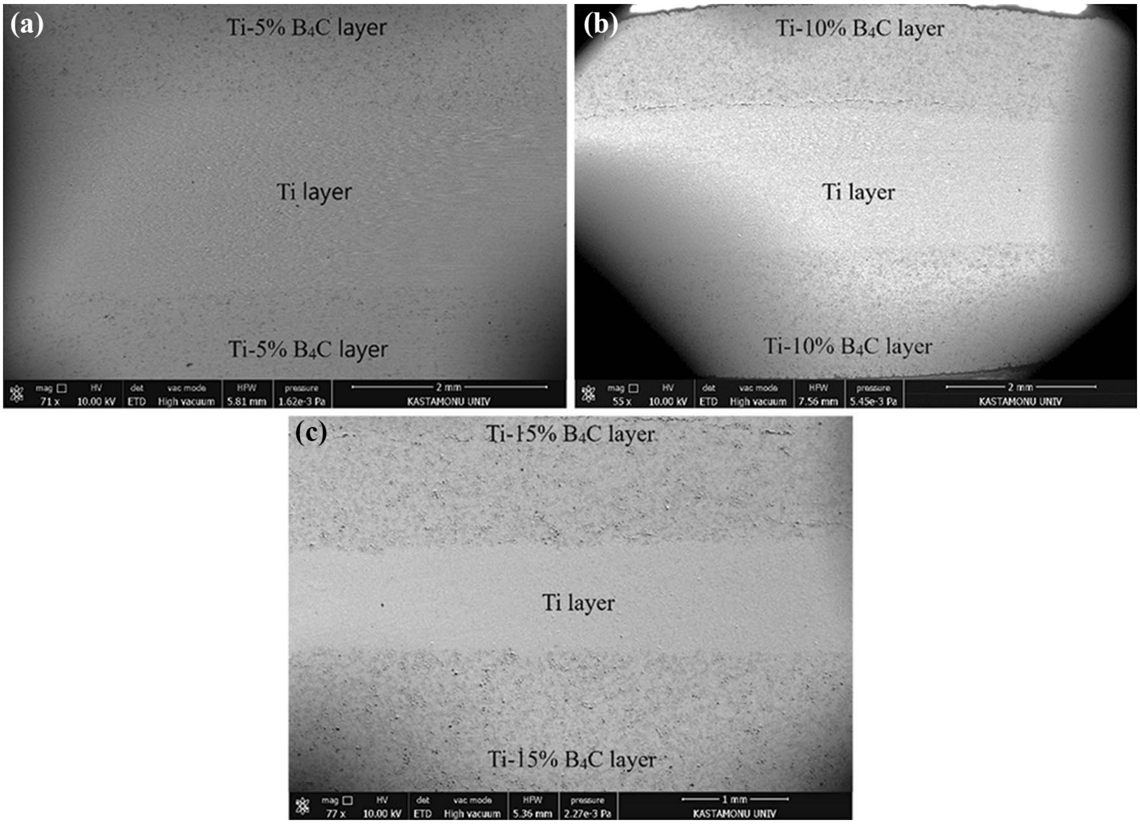

Fig. 3 General SEM images of FGMs: (**a**) sample 1, (**b**) sample 2, and (**c**) sample 3

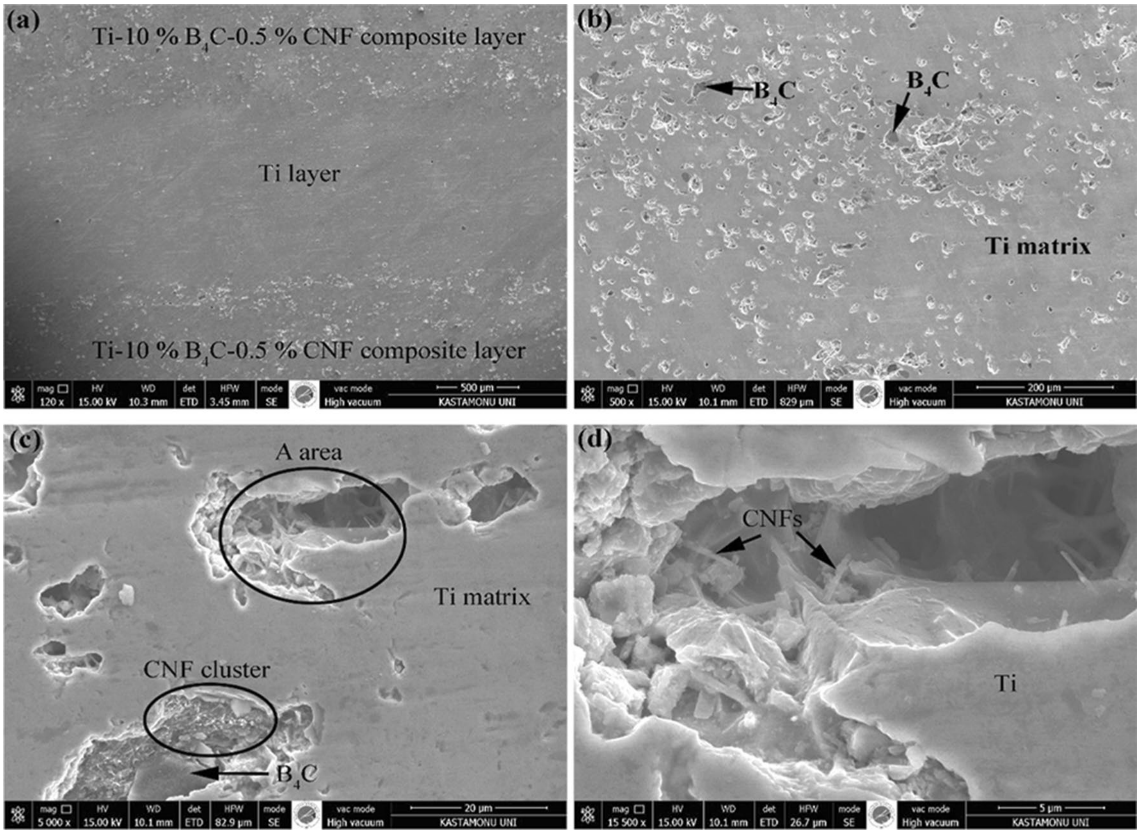

Fig. 4 SEM images of Ti-10% B_4C-0.5 CNF FGM: (**a**) three-layer view, (**b**) composite layer, (**c**) composite magnified view, and (**d**) region A

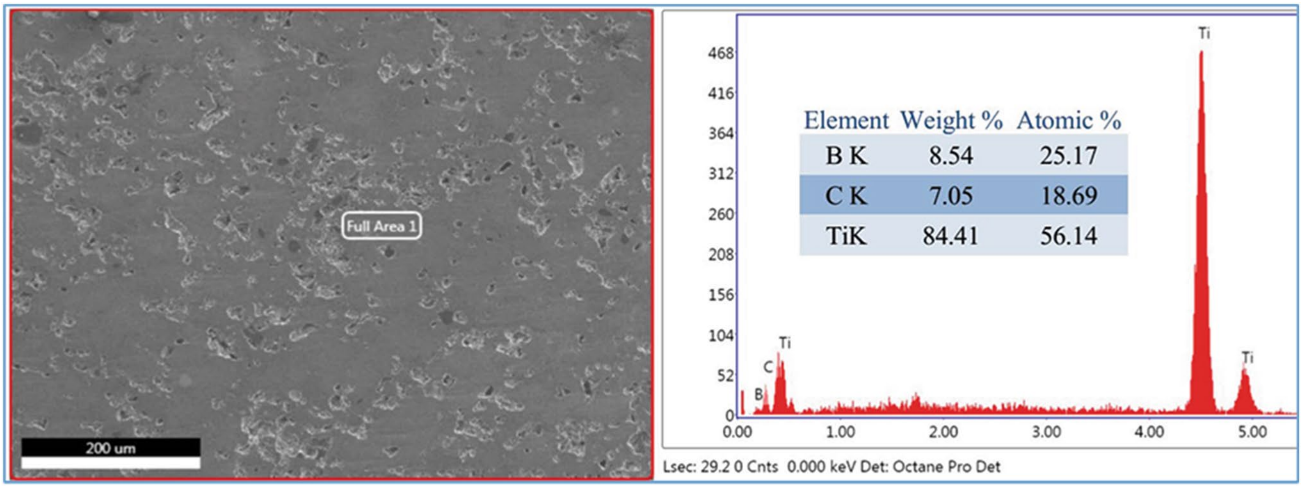

Element	Weight %	Atomic %
B K	8.54	25.17
C K	7.05	18.69
TiK	84.41	56.14

Fig. 5 EDS analysis of the composite layer of Ti-10% B_4C-0.5 CNF FGM

the layer, with carbon representing both the carbon in B_4C and the carbon in the CNFs.

In Fig. 6, an XRD analysis graph of the samples is given. XRD analyses were performed to determine whether any chemical interactions occurred between the powders involved in material production and the atmosphere. It is important to note such interactions because newly formed phases cause microstructural changes, thus altering a material's mechanical properties [15, 16]. The upper surfaces of the composite layers were also analyzed. According to the XRD analysis graph, Ti, B_4C, C, and TiB phases were formed within the microstructure. While Ti, B_4C, and C are the components used in material production, TiB is a newly formed phase. Previously, Li et al. [17] identified this new phase in a study on (TiC–TiB)/Ti composites. The authors reported that these phases occurred as a result of chemical reactions between Ti and B_4C. In our study, the peak intensity of this phase increased as the amount of B_4C in the composite increased. Further, it can be clearly seen from the XRD graph that no oxide formation occurs. Because a very small amount of CNF was present in the composite, it was not detected in most samples during XRD analysis, appearing in just FGM sample 5. In addition, when the graph is analyzed, it is clear that the Ti, TiB, and B_4C phases are dominant. During the sintering process, the TiB and B_4C phases resulted from the Ti, C, and B elements. A very small amount of the C phase was observed. As the amounts of Ti and B_4C added to the mix increased, the intensities of the B_4C and TiB phases increased [18].

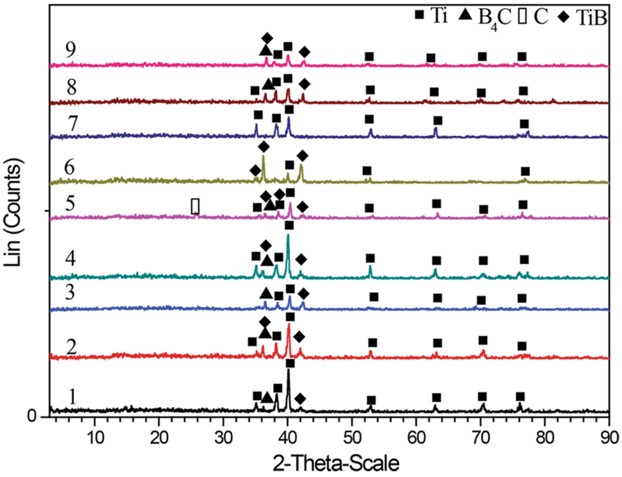

Fig. 6 XRD analysis graph of the samples

The theoretical densities, experimental densities, relative densities, and porosities of the samples are given in Fig. 7. The theoretical densities of the produced samples were calculated using Eq. 1 below.

$$\rho_{\mathrm{th}} = V_{\mathrm{Ti}}\rho_{\mathrm{Ti}} + V_{\mathrm{B4C}}\rho_{\mathrm{B4C}} + V_{\mathrm{CNF}}\rho_{\mathrm{CNF}}\left(\mathrm{g/cm^3}\right) \tag{1}$$

Here, ρ_{th} is the theoretical density of the final sample. The theoretical density of Ti is ρ_{Ti} (4.506 g/cm^3), the theoretical density of B_4C is ρ_{B4C} (2.520 g/cm^3), and the theoretical density of CNF is ρ_{CNF} (1.900 g.cm^{-3}). V_{Ti}, V_{B4C}, and V_{CNF} are the volume fractions of the matrix and reinforcements, respectively [19]. The experimental densities of the samples were measured using Archimedes' principle. The relative densities of the samples were calculated using Eq. 2 below.

$$\rho_{\mathrm{re}} = \rho_{\mathrm{ex}}/\rho_{\mathrm{th}} \times 100(\%) \tag{2}$$

Here, ρ_{re} denotes the relative density (%), ρ_{ex} denotes the experimental density (g/cm^3), and ρ_{th} denotes the theoretical density (g/cm^3) [16]. The porosities of the samples were calculated using Eq. 3 below.

$$P = 1 - \rho_{\mathrm{re}} \times 100(\%) \tag{3}$$

Here, P denotes the porosity (%), and ρ_{re} is the relative density (%) [20]. With the addition of B_4C and CNF, the experimental densities of the samples decreased. These decreases are related to the fact that the densities of B_4C and CNF are lower than that of Ti. The relative densities, i.e., the proportions of theoretical and experimental densities, decreased with the addition of B_4C and CNF due

Fig. 7 Density and porosity values of the samples

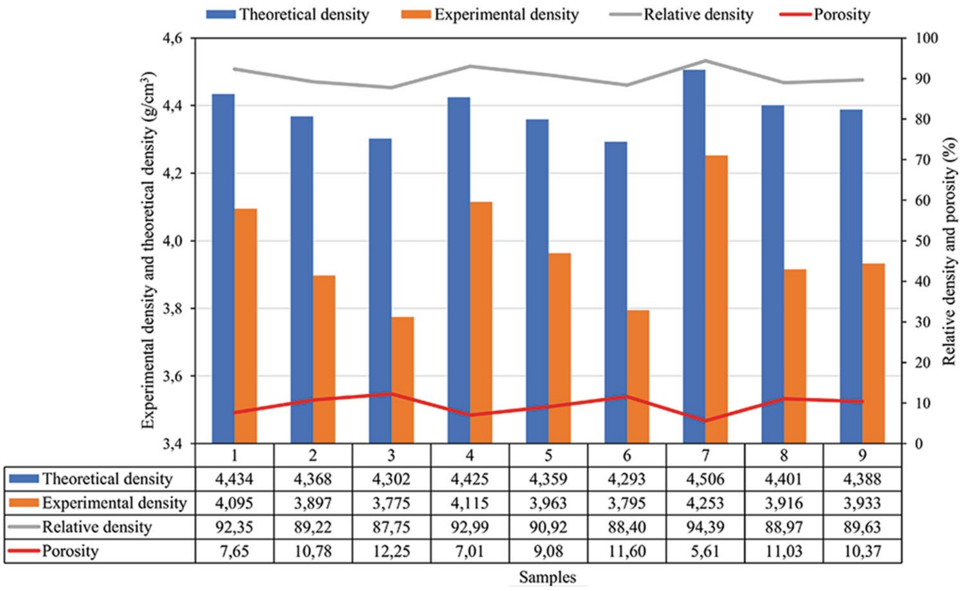

	1	2	3	4	5	6	7	8	9
Theoretical density	4,434	4,368	4,302	4,425	4,359	4,293	4,506	4,401	4,388
Experimental density	4,095	3,897	3,775	4,115	3,963	3,795	4,253	3,916	3,933
Relative density	92,35	89,22	87,75	92,99	90,92	88,40	94,39	88,97	89,63
Porosity	7,65	10,78	12,25	7,01	9,08	11,60	5,61	11,03	10,37

to the fact that increasing the B_4C ratio negatively affects compressibility [21]. However, because the CNFs partially enter the microvoids, the effect of reducing the relative densities is reduced. As a result, the increase in the B_4C ratio increased the porosities of the samples, while the CNF partially reduced these porosities.

The hardness values of the FGMs and bulk materials produced using the powder metallurgy method are given in Table 3. In FGMs, hardness measurements are taken from three layers, while, in bulk materials, measurements are taken from all surfaces. Five measurements were taken from different points in the layers and bulk materials. The averages of these measurements were then used to evaluate hardness. While the hardness of the middle layer was about 191 HV, the composite layer hardness values were 363, 453, and 510 HV for 5, 10, and 15% B_4C by volume, respectively. When 0.5% KNF by volume was added to these three samples, the hardness values increased to 385, 472, and 522 HV for 5, 10, and 15% B_4C by volume, respectively. The hardness values for the bulk samples with the same compositions as the FGMs were also measured. It is obvious that the hardness values for the materials increase with increases in the boron carbide amount and the addition of carbon nanofibers, which can be explained in several ways. First, the hardness values of B_4C and CNF reinforce that of the Ti matrix. Thus, hard reinforcements limit the plastic deformation of the composite and also increase its hardness. Second, the reinforcements in the Ti matrix play a role in preventing the movement of dislocations [22–25]. Third, the CNFs enter the pores and decrease porosity, thus increasing the hardness [26, 27]. The hardness values for the B_4C and CNF-reinforced samples are higher than that of the pure Ti sample. This increase is associated with the presence of carbides and the formation of hard phases. The addition of B_4C and CNF led to the formation of the TiB phase and consequently contributed to increases in hardness [28].

The TRS values obtained after the three-point bending test of the samples are given in Fig. 8. The TRS values of FGMs with Ti + 5% B_4C, Ti + 10% B_4C, Ti + 15% B_4C, Ti + 5% B_4C + 0.5CNF, Ti + 10% B_4C + 0.5CNF, and Ti + 15% B_4C + 0.5CNF compositions were found to be 610 MPa, 497 MPa, 379 MPa, 670 MPa, 525 MPa, and 439 MPa, respectively. The TRS values of the corresponding bulk materials were found to be 910 MPa, 492 MPa, and 505 MPa for Ti, Ti + 5% B_4C, and Ti + 5% B_4C + 0.5CNF, respectively. As the amount of B_4C added to the Ti matrix increased, the TRS values of both FGMs and bulk materials decreased due to the fact that the B_4C, with its high hardness, becomes more involved in the matrix, while, at the same time, cross-sectional weakening occurs in the matrix. In addition, the increase in porosity with the addition of B_4C is thought to lead to a decrease in the TRS value [29–31]. Significant increases in TRS values occurred when CNF was added to the Ti + B_4C composition, which can be explained by the strong bonding between the Ti matrix and the CNF. In other words, increases in TRS values were observed due to fiber bridging between the matrix and the fibers. When loaded, a crack forms in the matrix and progresses to the CNF. As the load increases, the CNF carries most of the load and fiber bridging occurs behind the cracked CNF. As the load increases further, the CNF undergoes plastic deformation and grains separate [32, 33]. FGMs produced by placing the pure titanium layer between the composite layers have a higher TRS than composite materials in bulk form. For example, the TRS of the Ti- 5% B_4C bulk composite material was 492 MPa, while that of Ti- 5% B_4C FGM was calculated as 610 MPa. While the hard particles in the composite layers triggered brittle fractures, the pure Ti intermediate layer absorbed energy and increased the TRS.

Table 3 Hardness values of the samples

Samples	Hardness ($HV_{0.2}$)		
	Upper layer	Middle layer	Lower layer
1 Ti-5 vol% B_4C	363	191	367
2 Ti-10 vol% B_4C	453	185	447
3 Ti-15 vol% B_4C	510	188	505
4 Ti-5 vol% B_4C-0.5 vol% CNF	385	182	379
5 Ti-10 vol% B_4C-0.5 vol% CNF	472	195	475
6 Ti-15 vol% B_4C-0.5 vol% CNF	522	182	519
7 Ti	190		
8 Ti-5 vol% B_4C	368		
9 Ti-5 vol% B_4C-0.5 vol% CNF	381		

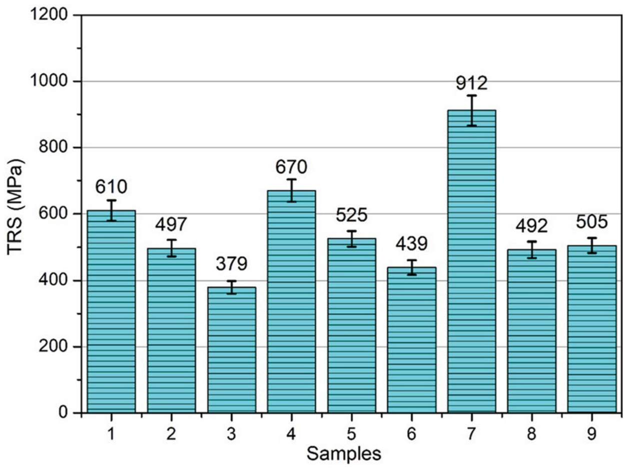

Fig. 8 TRS values of samples

Macro images showing crack progressions in FGM and bulk samples are shown in Fig. 9. In the bulk composite, cracks and fracturing occurred along the section, while, in the FGM sample, a crack occurred in the composite layer. This crack in the FGM advanced without any delamination between the layers.

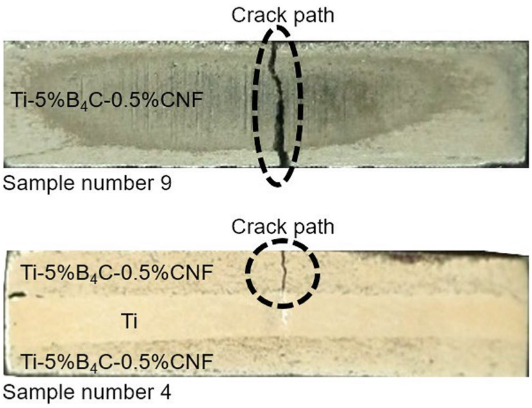

Fig. 9 Crack progression in FGM and bulk samples

After the three-point bending test, the fracture surfaces were examined using SEM. SEM images of the fracture surface of the Ti-15% B_4C-0.5% CNF FGM sample are shown in Fig. 10. According to the SEM image of the middle layer (Ti) in Fig. 10a, this layer exhibited a fracture morphology with a dimple-pit appearance. In addition, tearing back lines are visible in the micro image. Owing to this structure, Ti exhibits high plastic deformation. Figure 10b–d shows the fracture surface SEM images of the composite layer. Separation between unreacted B_4C particles and grains is seen in the fracture surface micrograph (Fig. 10b). Smaller dimple pits formed on the fractured surface of the composite layer than on the surface of the middle layer (Fig. 10c), which has been reported to be the result of the fixing effect of supplements [17]. Again, on the cracked surface, there are CNFs entering the Ti grain and also fracture TiB whiskers within the structure (Fig. 10d). This fracture phenomenon is related to the strong interface compatibility between the Ti matrix and TiB whiskers [34, 35].

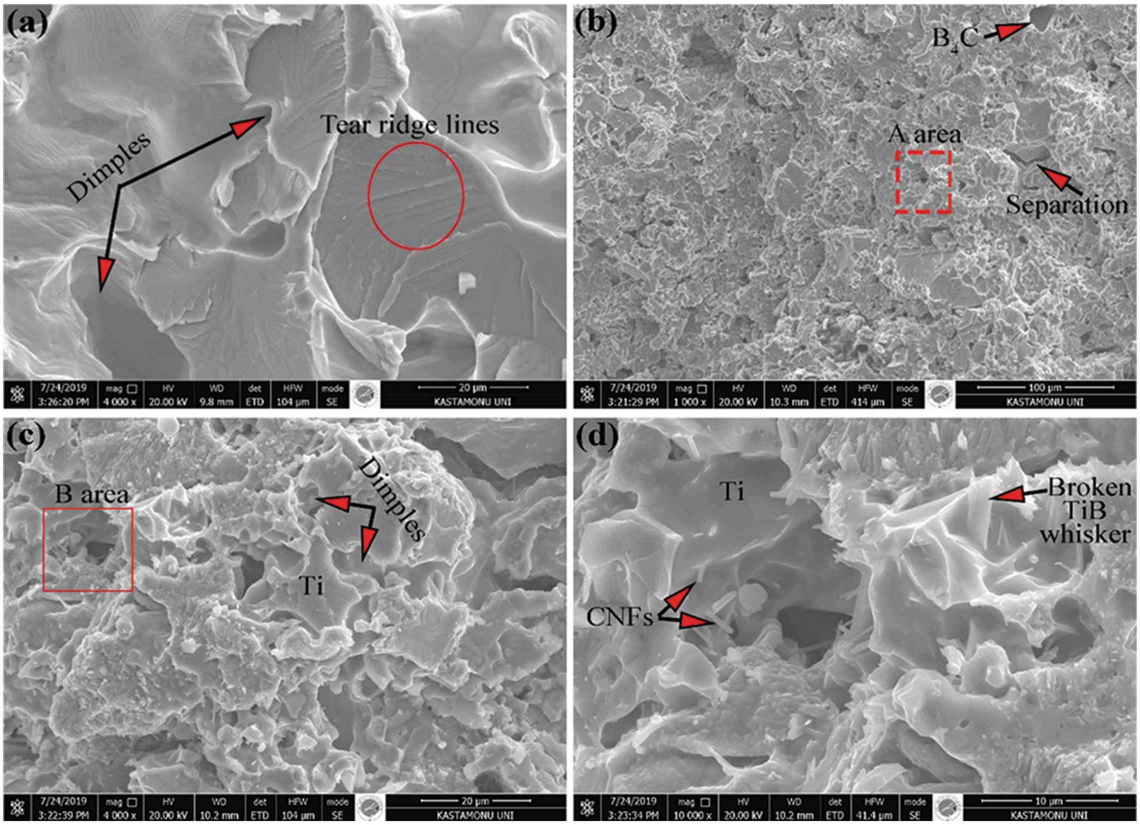

Fig. 10 SEM images of the fracture surface of the Ti-15% B_4C-0.5% CNF FGM sample: (**a**) middle layer, (**b**) composite layer, (**c**) A area, and (**d**) B area

Conclusions

In this study, Ti-B_4C/CNF FGMs were successfully produced using the powder metallurgy method. SEM–EDS, XRD, microhardness, density, and three-point bending tests were successfully conducted on the samples. The experimental results can be summarized as follows:

1. SEM images show that there is sufficient bonding between the layers making up the FGM and that the reinforcing elements are relatively homogeneously distributed within the matrix.
2. In addition to the Ti, B_4C, and C phases, which represent the powders in the structure according to the XRD patterns, a new TiB phase was formed. There was no oxide formation in the microstructure.
3. With the addition of B_4C and CNF, the experimental densities and relative densities of the samples decreased and the porosities increased. In addition, with increasing reinforcement, there was also a marked increase in the hardness values of the samples.
4. The addition of B_4C and CNF led to the formation of the TiB and B_4C phases, consequently increasing the hardness.
5. The TRS values of FGM-shaped samples were higher than those of their corresponding composite samples. The middle layer (Ti) increased the strength by absorbing energy during loading.

References

1. J. Ma, Z. He, G.E.B. Tan, Fabrication and characterization of Ti-TiB_2 functionally graded material system. Metall. Mater. Trans. A. **33**, 681–685 (2002)
2. M. Koizumi, FGM activities in Japan. Compos. B. Eng. **28**, 1–4 (1997)
3. F. Erdemir, A. Canakci, T. Varol, Microstructural characterization and mechanical properties of functionally graded Al2024/SiC composites prepared by powder metallurgy techniques. Trans. Nonferrous Met. Soc. China. **25**, 3569–3577 (2015)
4. F. Erdemir, A. Canakci, T. Varol, S. Ozkaya, Corrosion and wear behavior of functionally graded Al2024/SiC composites produced by hot pressing and consolidation. J. Alloys Compd. **644**, 589–596 (2015)
5. R.M. Mahamood, E.T. Akinlabi, Future research direction in functionally graded materials and summary. in *Functionally Graded Materials. Topics in Mining, Metallurgy and Materials Engineering*. (Springer, Cham, 2017) pp. 93–103
6. H.S. Hedia, N. Fouda, A new design of dental implant coating using functionally graded material. Mater. Test. **55**, 765–771 (2013)
7. S.C. Tjong, Y.W. Mai, Processing-structure-property aspects of particulate- and whisker-reinforced titanium matrix composites. Compos. Sci. Technol. **68**, 583–601 (2008)
8. Z. Zhang, J. Qin, Z. Zhang, Y. Chen, W. Lu, D. Zhang, Effect of β heat treatment temperature on microstructure and mechanical properties of in situ titanium matrix composites. Mater. Des. **31**, 4269–4273 (2010)
9. H. Duan, Y. Han, W. Lu, L. Wang, J. Mao, D. Zhang, Configuration design and fabrication of laminated titanium matrix composites. Mater. Des. **99**, 219–224 (2016)
10. K. Kondoh, *Titanium Metal Matrix Composites by Powder Metallurgy (PM) Routes. Titanium Powder Metallurgy* (Butterworth-Heinemann, Oxford, 2015), pp. 277–297
11. A. Muthuchamy, G.D.J. Ram, V.S. Sarma, Spark plasma consolidation of continuous fiber reinforced titanium matrix composites. Mat. Sci. Eng. A. **703**, 461–469 (2017)
12. C.J. Zhang, F.T. Kong, L.J. Xu, E.T. Zhao, S.L. Xiao, Y.Y. Chen, N.J. Deng, W. Ge, G.J. Xu, Temperature dependence of tensile properties and fracture behavior of as rolled TiB/Ti composite sheet. Mat. Sci. Eng. A. **556**, 962–969 (2012)
13. H. Xu, Q. Li, Effect of carbon nanofiber concentration on mechanical properties of porous magnesium composites: experimental and theoretical analysis. Mat. Sci. Eng. A. **706**, 249–255 (2017)
14. M.G. Randal, *Powder Metallurgy and Particulate Materials Processing, Metal Powder Industry* (2005)
15. L.I. Shufeng, K. Kondoh, H. Imai, B. Chen, L. Jia, J. Umeda, Microstructure and mechanical properties of P/M titanium matrix composites reinforced by in-situ synthesized TiC–TiB. Mat. Sci. Eng. A. **628**, 75–83 (2015)
16. A.S. Namini, M. Azadbeh, M.S. Asl, Effect of TiB_2 content on the characteristics of spark plasma sintered Ti–TiB_w composites. Adv. Powder Technol. **28**, 1564–1572 (2017)
17. S. Li, K. Kondoh, H. Imai, B. Chen, L. Jia, J. Umeda, Y. Fu, Strengthening behavior of in situ-synthesized (TiC–TiB)/Ti composites by powder metallurgy and hot extrusion. Mater. Des. **95**, 127–132 (2016)
18. M. Nazarian-Samani, A.R. Kamali, R. Mobarra, Phase transformations of Ni-15 wt.% B powders during mechanical alloying and annealing. Mater. Lett. **64**, 309–312 (2010)
19. S. Islak, Effect of sintering parameters on sawing performance of marble cutting tools with carbide, PhD thesis, Firat University, Turkey (2012).
20. I.N. Popescu, S. Zamfir, V.F. Anghelina, C.O. Rusanescu, Processing by P/M route and characterization of new ecological aluminum matrix composites (AMC). Int. J. Mech. **4**, 43–52 (2010)
21. M. Rahimian, N. Ehsani, N. Parvin, H.R. Baharvandi, The effect of particle size, sintering temperature and sintering time on the properties of Al–Al_2O_3 composites, made by powder metallurgy. J. Mater. Process. Technol. **209**, 5387–5393 (2009)
22. S.A. Sajjadi, H.R. Ezatpour, H. Beygi, Microstructure and mechanical properties of Al–Al_2O_3 micro and nano composites fabricated by stir casting. Mat. Sci. Eng. A. **528**, 8765–8771 (2011)
23. M. Rahimian, N. Parvin, N. Ehsani, Investigation of particle size and amount of alumina on microstructure and mechanical properties of Al matrix composite made by powder metallurgy. Mat. Sci. Eng. A. **527**, 1031–1038 (2010)
24. S. Buytoz, F. Dağdelen, S. Islak, M. Kök, D. Kır, E. Ercan, Effect of the TiC content on microstructure and thermal properties of Cu–TiC composites prepared by powder metallurgy. J. Therm. Anal. Calorim. **117**, 1277–1283 (2014)
25. S. Islak, Mechanical and corrosion properties of AlCu matrix hybrid composite materials. Sci. Sinter. **51**, 81–92 (2019)
26. M.M.H. Bastwros, A.M.K. Esawi, A. Wifi, Friction and wear behavior of Al–CNT composites. Wear. **307**, 164–173 (2013)
27. S. Islak, Ö. Küçük, Ö. Eski, C. Özorak, M. Akkaş, The effect of CNT content and sintering temperature on some properties of CNT-reinforced MgAl composites. Sci. Sinter. **49**, 347–357 (2017)

28. K. Otsuka, X. Ren, Physical metallurgy of Ti–Ni-based shape memory alloys. Prog. Mater. Sci. **50**, 511–678 (2005)
29. X. Jin, L. Wu, Y. Sun, L. Guo, Microstructure and mechanical properties of ZrO2/NiCr functionally graded materials. Mat. Sci. Eng. A. **509**, 63–68 (2009)
30. J. Dwan, Fracture toughness determination of diamond impregnated PM cobalt. Ind. Diamond Rev. **1**, 33–36 (2007)
31. S. Islak, H. Çelik, Effect of sintering temperature and boron carbide content on the wear behavior of hot pressed diamond cutting segments. Sci. Sinter. **47**, 131–143 (2015)
32. Y. Chen, S. Wang, B. Liu, J. Zhang, Effects of geometrical and mechanical properties of fiber and matrix on composite fracture toughness. Compos. Struct. **122**, 496–506 (2015)
33. C.R. Chiang, Prediction of the fracture toughness of fibrous composites. J. Mater. Sci. **35**, 3161–3166 (2000)
34. H. Singh, M. Hayat, Z. He, V.K. Peterson, R. Das, P. Cao, In situ neutron diffraction observations of Ti-TiB composites. Compos. Part A-Appl. S. **124**, 105501 (2019)
35. Z. Yan, F. Chen, Y. Cai, Y. Zheng, Microstructure and mechanical properties of in-situ synthesized TiB whiskers reinforced titanium matrix composites by high-velocity compaction. Powder Technol. **267**, 309–314 (2014)